Rev. Roum. Sci. Techn.– Électrotechn. et Énerg.
Vol. **71**, *4*, pp. 513–518, Bucarest, 2026

PROCESSOR-IN-THE-LOOP VALIDATION OF SENSORLESS DIRECT TORQUE CONTROL FOR PARALLEL FIVE-PHASE PMSM DRIVES

MAAMAR SOUAIHIA[1], KAMEL TOUNSI [1]

Keywords: Five-phase permanent magnet synchronous machine (PMSM); Parallel-connected drives; Direct torque control with space vector modulation (DTC-SVM); Model reference adaptive system (MRAS); Sensorless control; Processor-in-the-loop.

This paper presents a sensorless model reference adaptive system (MRAS) speed and position estimator embedded in a direct torque control with space vector modulation (DTC-SVM) scheme for two five-phase permanent magnet synchronous machines (PMSMs) connected in parallel to a single five-phase inverter. The MRAS jointly estimates rotor speed, position, torque, and stator flux for each machine, removing the need for mechanical sensors while keeping the two drives fully decoupled despite sharing one inverter. The scheme is validated experimentally through processor-in-the-loop (PIL) co-simulation, running the control algorithm on an STM32F407 Discovery board coupled to a MATLAB/Simulink SimPowerSystems plant model over a UART link. Across four test scenarios — co-directional speed tracking, counter-rotating operation, alternating high-speed reversal, and low-speed operation — the estimator tracks the reference speeds closely (peak transient error below 0.1 rad/s, settling below 0.02 rad/s at low speed), the stator flux remains constant near 0.3 Wb, and the two machines remain fully decoupled: load, speed, or direction changes on one drive produce no measurable disturbance on the other.

1. INTRODUCTION

Five-phase machines are increasingly preferred over their three-phase counterparts in high-power applications: splitting the same power across more phases lowers the per-phase current rating, reduces torque ripple, and - crucially - lets the drive keep running on the remaining phases if one leg fails [1]. Combined with the high efficiency, favorable torque-to-inertia ratio, and compact size of permanent magnet synchronous machines (PMSMs), five-phase PMSMs are now common in electric vehicles, aircraft, marine propulsion, and industrial servo drives [2].

High-power applications such as traction and propulsion often need two or more machines working together [3]. Feeding each machine from its own inverter is straightforward but doubles the power-electronics cost and footprint. An attractive alternative, used in this paper, connects two five-phase PMSMs in parallel to a single five-phase inverter through a fixed phase-transposition wiring, which, as shown in Section 2, maps each machine onto its own orthogonal subspace of the inverter's control variables, so the two machines can still be commanded independently [4,6].

For the control law itself, direct torque control (DTC) is attractive because it needs no Park transformation and no precise machine parameters, and it responds fast to torque-command changes. Classic lookup-table DTC, however, suffers from high torque ripple and a variable switching frequency; combining DTC with space vector modulation (DTC-SVM) fixes both issues by imposing a constant switching frequency while preserving DTC's fast dynamics [7–9].

DTC-SVM needs the rotor speed for its feedback loop. Mechanical sensors (encoders, resolvers) are fragile, add cost, and increase wiring complexity, which motivates sensorless (observer-based) speed estimation [10–12]. Among the available techniques, the Extended Kalman Filter gives good tracking but is computationally heavy and needs careful parameter tuning; sliding-mode observers are robust but suffer from chattering unless a super-twisting algorithm is added, which again increases complexity [13]. A model reference adaptive system (MRAS) offers a good compromise: it is algorithmically simple, computationally light, and its stability can be established directly with a Lyapunov argument, which is why it is adopted here for the parallel two-machine drive [14].

Before any control law is trusted on real power hardware, it is good practice to validate the embedded implementation against a virtual plant. Processor-in-the-loop (PIL) prototyping does exactly this: the control algorithm runs on the real target microcontroller while the power stage and machines are simulated on a host PC, with the two communicating in non-real time. This exposes implementation issues - fixed-point effects, execution time, code size - that a purely offline simulation cannot, without the cost or risk of a full experimental rig [15]. STM32-family boards are the most widely reported PIL target in the literature, mainly because of their low cost, adequate clock speed, and straightforward toolchain integration with Simulink's embedded coder [16,17].An STM32F407 Discovery board is used here for the same reasons.

This paper combines the three elements above, a parallel-connected two five-phase PMSM drive fed by a single inverter, a dual per-machine MRAS estimator supplying speed, position, torque, and flux to a DTC-SVM control loop, and PIL validation on an STM32F407 board, and evaluates the resulting sensorless drive over four representative operating scenarios: co-directional speed tracking, counter-rotating operation, alternating high-speed reversal, and low-speed operation.

2. DRIVE SYSTEM AND MACHINE MODEL

2.1 PARALLEL FIVE-PHASE TOPOLOGY

Figure 1 shows the two five-phase PMSMs connected in parallel to a single five-phase voltage-source inverter (VSI). Direct parallel connection of two five-phase windings would leave the machines' currents coupled through the shared inverter legs; the fixed phase-transposition wiring (as1–as2, bs1–cs2, cs1–es2, ds1–bs2, es1–ds2) [7] removes this coupling,

$$[C]=\frac{2}{5}\begin{bmatrix} \cos\theta & \cos\left(\theta-\frac{2\pi}{5}\right) & \cos\left(\theta-\frac{4\pi}{5}\right) & \cos\left(\theta+\frac{4\pi}{5}\right) & \cos\left(\theta+\frac{2\pi}{5}\right) \\ \sin\theta & \sin\left(\theta-\frac{2\pi}{5}\right) & \sin\left(\theta-\frac{4\pi}{5}\right) & \sin\left(\theta+\frac{4\pi}{5}\right) & \sin\left(\theta+\frac{2\pi}{5}\right) \\ \cos\theta & \cos\left(\theta-\frac{4\pi}{5}\right) & \cos\left(\theta+\frac{2\pi}{5}\right) & \cos\left(\theta-\frac{2\pi}{5}\right) & \cos\left(\theta+\frac{4\pi}{5}\right) \\ \sin\theta & \sin\left(\theta-\frac{4\pi}{5}\right) & \sin\left(\theta+\frac{2\pi}{5}\right) & \sin\left(\theta-\frac{2\pi}{5}\right) & \sin\left(\theta+\frac{4\pi}{5}\right) \\ \frac{1}{2} & \frac{1}{2} & \frac{1}{2} & \frac{1}{2} & \frac{1}{2} \end{bmatrix}. \quad (1)$$

[1] Electrical Engineering Department, LGEER Laboratory, University of Chlef, Algeria.
E-mails:m.souaihia@univ-chlef.dz, ka.tounsi@univ-chlef.dz

DOI: 10.59277/RRST-EE.2026.4.6

The five-phase stator variables of each machine are mapped into the d-q-x-y-0 frame with the transformation matrix (1); machine 1 occupies the d-q subspace and machine 2 the x-y subspace of that same frame — so the two machines can be torque- and flux-controlled independently from one inverter, which is the basis of the whole control structure in Section 3.

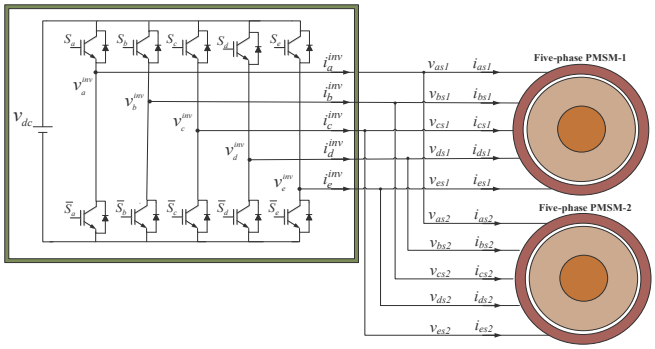


Fig. 1 –Two five-phase PMSMs connected in parallel to a single five-phase voltage-source inverter (VSI).

2.2 FIVE-PHASE PMSM MODEL

In the rotating d-q-x-y frame, the stator-voltage equations of each machine j (j = 1, 2) are:

$$\begin{aligned} v_{dsj} &= -r_{sj}i_{dsj} - \frac{L_{dj}\mathrm{d}i_{dsj}}{\mathrm{d}t} + \omega_j L_{qj} i_{qsj} \\ v_{qsj} &= -r_{sj}i_{qsj} - \frac{L_{qj}\mathrm{d}i_{qsj}}{\mathrm{d}t} - \omega_j L_{dj} i_{dsj} - \omega_j \Phi_{fj} \\ v_{xsj} &= -r_{sj}i_{xsj} - \frac{L_{lsj}\mathrm{d}i_{xsj}}{\mathrm{d}t} \\ v_{ysj} &= -r_{sj}i_{ysj} - \frac{L_{lsj}\mathrm{d}i_{ysj}}{\mathrm{d}t} \end{aligned} \qquad (2)$$

where v_{dj}, v_{qj}, v_{xj}, v_{yj} and i_{dj}, i_{qj}, i_{xj}, i_{yj} are the stator voltages and currents; L_{dj}, L_{qj}, L_{lsj} are the d, q, and leakage inductances; r_{sj} is the stator resistance; Φ_{fj} is the permanent-magnet flux; and ω_j, θ_j are the electrical speed and rotor position. The minus signs in (2) follow one fixed sign convention, used the same way for every term, in every equation in this paper. The electromagnetic torque and mechanical motion are given as:

$$\begin{aligned} T_{emj} &= \frac{5p_j}{2}\left[\Phi_{fj} i_{qj} + \left(L_{dj} - L_{qj}\right) i_{qj} i_{dj}\right], \\ T_{mj} - T_{emj} &= \frac{J_j \mathrm{d}\Omega_j}{\mathrm{d}t}, \end{aligned} \qquad (3)$$

where $p_{j\,is}$ the pole-pair count, J_j is the rotor inertia, $\Omega_{j\,is}$ the mechanical speed, and $T_{m,j}$ is the applied mechanical torque.

3. PROPOSED DTC-SVM / MRAS CONTROL STRUCTURE

Figure 2 shows the overall control structure. Each machine has its own DTC-SVM loop: a speed PI regulator produces the torque reference, a flux PI regulator produces the flux reference, and both are converted — using the estimated rotor position — into voltage references in the machine's own subspace (z_1–z_2 to αβ for machine 1, z_3–z_4 to x-y for machine 2). The two voltage references are modulated by a shared SVM stage and combined by a single switching-signal-selection block that drives the common five-phase VSI. Each loop is closed by its own estimator (explained in Section 3.1), which reconstructs speed, position, torque, and flux for its machine from the measured stator voltages and currents, so no mechanical sensor is required on either machine.

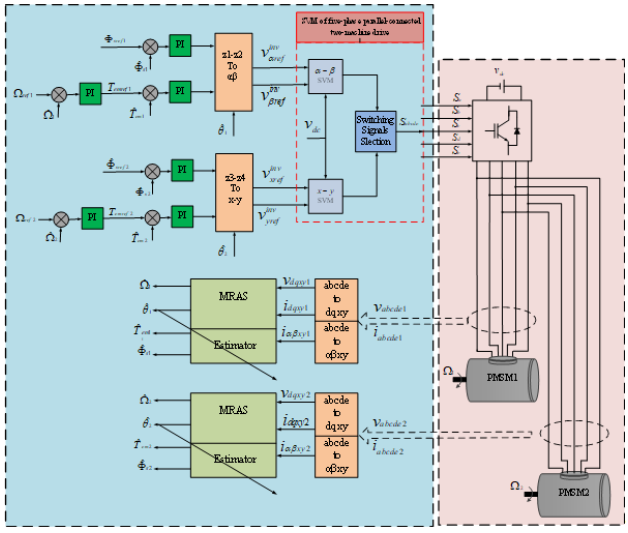


Fig. 2 – Overall DTC-SVM control structure with dual per-machine MRAS estimators for the parallel-connected two five-phase PMSM drive.

3.1 MRAS-BASED SPEED AND POSITION ESTIMATOR

Figure 3 details the MRAS estimator used on each machine. The real machine (fed the measured voltages V_{abcde}) acts as the reference model, producing the measured currents I_{abcde}; an adjustable model, driven by the same voltages and the current speed estimate, predicts the same currents in the d-q-x-y frame. The current-estimation error $e = i_{dqxy} - \hat{i}_{dqxy}$ drives a PI-type adaptation law that updates the speed estimate $\hat{\omega}$, which is then integrated to give the position estimate $\hat{\theta}$.

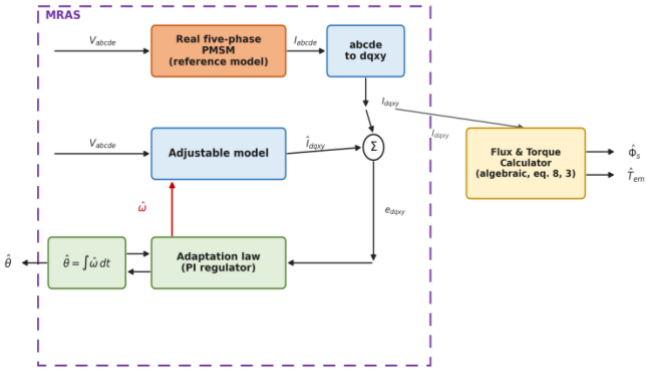


Fig. 3 – Block diagram of the Estimator: the MRAS (reference model, adjustable model, and adaptation law) gives the speed and position estimates, while the separate flux & torque calculator gives the flux and torque estimates, matching the four outputs of Fig. 2.

The reference model in Fig. 3 is the real machine.

$$\begin{aligned} L_{dj}\frac{\mathrm{d}\hat{i}_{dsj}}{\mathrm{d}t} &= -r_{sj}\hat{i}_{dsj} + \hat{\omega}_j L_{qj}\hat{i}_{qsj} - v_{dsj}, \\ L_{qj}\frac{\mathrm{d}\hat{i}_{qsj}}{\mathrm{d}t} &= -r_{sj}\hat{i}_{qsj} - \hat{\omega}_j L_{dj}\hat{i}_{dsj} - \hat{\omega}_j \Phi_{fj} - v_{qsj}, \\ L_{lsj}\frac{\mathrm{d}\hat{i}_{xsj}}{\mathrm{d}t} &= -r_{sj}\hat{i}_{xsj} - v_{xsj}, \\ L_{lsj}\frac{\mathrm{d}\hat{i}_{ysj}}{\mathrm{d}t} &= -r_{sj}\hat{i}_{ysj} - v_{ysj}. \end{aligned} \qquad (4)$$

It is driven by the measured voltages and gives the measured currents, exactly as in (2). The adjustable model copies the same structure in software: it uses the same

measured voltages and the same fixed (nameplate) values of r_{sj}, L_{dj}, L_{qj}, L_{lsj}, Φ_{fj}, but it uses the speed estimate $\hat{\omega}_j$ instead of the real, unknown speed. Its four equations are given in eq. (4).

Using the reference model (2) and the adjustable model (4), both written in state-space form, and subtracting one from the other gives the error dynamics:

$$\begin{bmatrix}\dot{\hat{e}}_{dj}\\ \dot{\hat{e}}_{qj}\\ \dot{\hat{e}}_{xj}\\ \dot{\hat{e}}_{yj}\end{bmatrix}=\begin{bmatrix}\frac{r_{sj}}{L_{dj}} & \left(\frac{L_{qj}}{L_{dj}}\right)\hat{\omega}_j & 0 & 0\\ \left(\frac{L_{dj}}{L_{qj}}\right)\hat{\omega}_j & \frac{r_{sj}}{L_{qj}} & 0 & 0\\ 0 & 0 & \frac{r_{sj}}{L_{lsj}} & 0\\ 0 & 0 & 0 & \frac{r_{sj}}{L_{lsj}}\end{bmatrix}\begin{bmatrix}\hat{e}_{dj}\\ \hat{e}_{qj}\\ \hat{e}_{xj}\\ \hat{e}_{yj}\end{bmatrix}+\begin{bmatrix}\left(\frac{L_{qj}}{L_{dj}}\right)\hat{\imath}_{qj}\\ -\frac{\Phi_{fj}-L_{dj}\hat{\imath}_{dj}}{L_{qj}}\\ 0\\ 0\end{bmatrix}(\omega_j-\hat{\omega}_j). \quad (5)$$

Asymptotic convergence of the observer error is established with the Lyapunov candidate $V = e^{T}e+(\omega_j-\hat{\omega}_j)^2/\lambda$ ($\lambda > 0$); V is positive definite, while its time derivative is negative semidefinite when the adaptation law is chosen to cancel the cross term [9]. This standard Lyapunov-based MRAS derivation (omitted here for brevity) yields the practical, PI-regulated adaptation law implemented:

$$\hat{\omega}_j = k_p\left[e_{dj}\left(\frac{L_{qj}}{L_{dj}}\right)i_{qj}-\frac{e_{qj}(\Phi_{fj}+L_{dj}i_{dj})}{L_{qj}}\right]+ k_i\int\left[e_{dj}\left(\frac{L_{qj}}{L_{dj}}\right)i_{qj}-\frac{e_{qj}(\Phi_{fj}+L_{dj}i_{dj})}{L_{qj}}\right]dt, \quad (6)$$

with k_p, k_i the adaptation-law gains. The rotor position estimate is then obtained by integration:

$$\hat{\theta}_j = \int \hat{\omega}_j\, dt. \quad (7)$$

The estimator in Fig. 2 has two parts. The first part is the MRAS of Fig. 3: reference model, adjustable model (4), and adaptation law (6). It gives only the speed estimate and, by integration (7), the position estimate; no sensor and no extra model are needed. The second part is simpler: at every sample, it computes the stator-flux size directly from the measured currents and the known machine parameters - no adjustable model is needed for this. The flux estimate comes from (8), and the torque estimate is computed the same way, using the measured currents in (3). Figure 3 shows only the first part (speed and position), to keep the figure clear; the second part (flux and torque) is shown as a separate block, and together the two parts form the estimator of Fig. 2,

$$\hat{\Phi}_{sj} = \sqrt{\left(L_{dj}\hat{\imath}_{dsj}+\Phi_{fj}\right)^2+\left(L_{qj}\hat{\imath}_{qsj}\right)^2}. \quad (8)$$

4. PROCESSOR-IN-THE-LOOP VALIDATION SETUP

Before committing the control algorithm to real power hardware, it is validated by processor-in-the-loop (PIL) co-simulation: the control code runs on the target microcontroller while the power stage and the two PMSMs are simulated on a host PC, with the two exchanging inputs/outputs over a non-real-time link (Fig. 4).

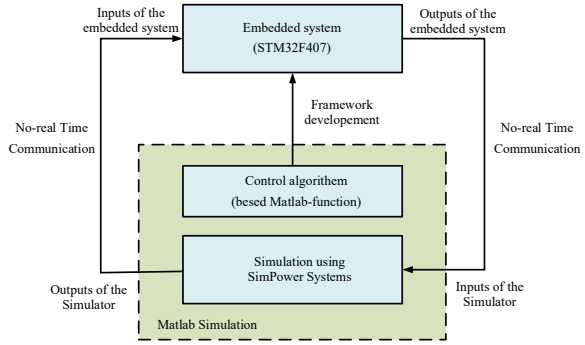


Fig. 4 – Principle of processor-in-the-loop (PIL) co-simulation: the embedded controller and the host-simulated plant exchange data in non-real time.

This exposes embedded-implementation effects — code size, memory footprint, execution turnaround — that a purely offline Simulink simulation cannot, and lets the algorithm be refined before any hardware risk is taken [18].

Figure 5 summarizes the configuration steps, and Fig. 6 shows the resulting hardware/software partition: the board exchanges data with the host over UART through an FTDI232 USB-to-serial converter, sending back the measured currents/voltages of both machines and receiving the switching commands.

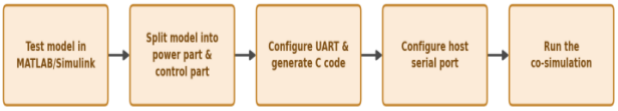


Fig. 5 – Hardware/software partition: control part on the STM32F407 Discovery board, power circuit part simulated in MATLAB/Simulink, linked via an FTDI232 UART bridge.

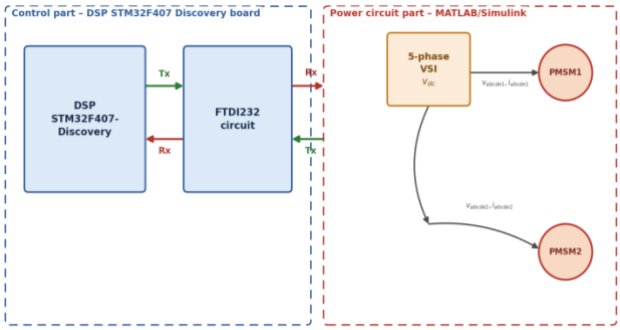


Fig. 6 – Hardware/software partition: control part on the STM32F407 Discovery board, power circuit part simulated in MATLAB/Simulink, linked via an FTDI232 UART bridge.

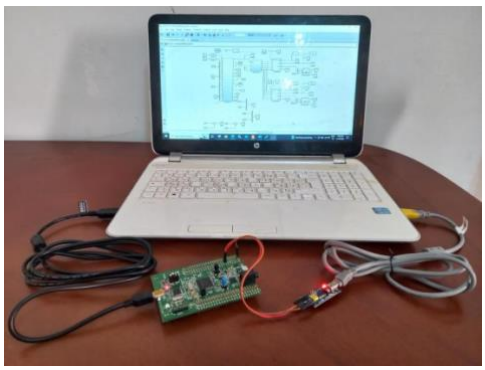


Fig. 7 – PIL test bench: STM32F4-Discovery board, FTDI232 converter, and host PC running the Simulink plant model.

The target is an STM32F407 Discovery board (32-bit Cortex-M4, 168 MHz, 1 MB flash, 192 kB SRAM), chosen for its low cost and straightforward integration with

Simulink's Embedded Coder. The control algorithm is developed as a MATLAB Function block, auto-generated to C code, and flashed to the board; the power circuit (five-phase VSI and the two PMSMs) is kept in Simulink/SimPowerSystems on the host.

5. SIMULATION AND PIL RESULTS

The proposed control was implemented with MATLAB embedded functions and co-simulated through the PIL link described in Section 4, using two identical five-phase PMSMs whose parameters are listed in Table 1. Four scenarios were used to stress-test the sensorless drive: co-directional speed tracking, counter-rotating operation, alternating high-speed reversal, and low-speed operation. Table 2 summarizes the key metrics across all four; each is then discussed with its corresponding figure.

Table 1

Five-phase PMSM parameters.

Parameter	Value
Pole pairs	5
Stator resistance, rs (Ω)	1.09
d-axis inductance, Ld,Lq (H)	0.0124
Rotor inertia, J (kg·m²)	4.15×10^{-4}
Magnet flux, Φ_f (Wb)	0.3

Table 1 gives one inductance value because the simulated machines are non-salient ($L_d = L_q$). The control law in Section 3 and the model in (2),(3) are written for the general, salient case, but the tests in Section 5 use non-salient machines only. This is a simplification, not a limit of the method: when $L_d = L_q$, the term $(L_{dj} - L_{qj})$ in (3), and the cross terms in (2), (4), and (5), simply become zero. Testing the general, salient case is left for future work.

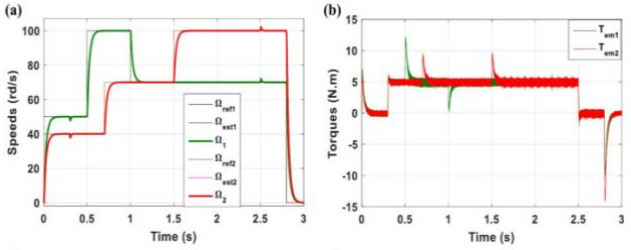
Table 2

Summary of the Four PIL test scenarios.

Test	Scenario
1	Co-directional, multi-step speeds (40–100 rad/s), nominal load at t = 0.3
2	Counter-rotating operation (±50 to ±90 rad/s)
3	*Alternating high-speed reversal,* 0.5s *cycle* (0 / 100 rad/s)
4	*Low-speed operation* (–15 to +15 rad/s)

5.1 CO-DIRECTIONAL OPERATION

With no load at start-up, machine 1 is stepped through 50, 100 and 70 rad/s (t = 0, 0.5, 1 s) and machine 2 through 40, 70 and 100 rad/s (t = 0, 0.7, 1.5 s); both machines are loaded with their nominal torque at t = 0.3 s and brought to standstill at t = 2.8 s. Figure 8 shows both machines tracking their references closely, with the estimated and measured speeds overlapping throughout.



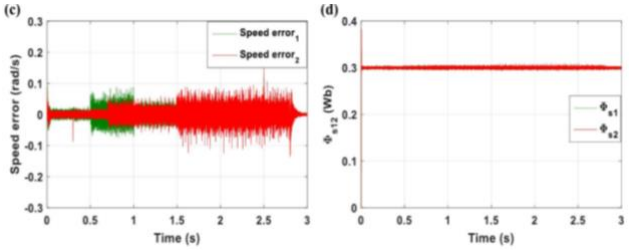


Fig. 8 – Co-directional operation: (a) reference/estimated/actual speeds, (b) electromagnetic torques, (c) speed-estimation errors, (d) stator flux magnitudes.

The speed error grows only during the step transitions (peak ≈ 0.1 rad/s) and decays as the two speeds settle; torque starts near 10 N·m at start-up, drops to zero at the t = 0.3 s load step, then holds around 5 N·m until the machines are stopped. Stator flux stays essentially constant at 0.3 Wb throughout.

5.2 COUNTER-ROTATING OPERATION

Machine 1 accelerates to +100 rad/s while machine 2 runs at −50 rad/s; both reverse direction at t = 1 s (to −90 and +90 rad/s, respectively), return to zero at t = 2 s, and are then both set to +50 rad/s at t = 2.5 s. As Fig. 9 shows, the direction reversal of one machine leaves the other's speed and torque trace visibly undisturbed, and the speed error (peak ≈ 0.05 rad/s) tracks the same transient pattern independently on each machine. Torque again settles around 5 N·m between transients, and flux remains at 0.3 Wb.

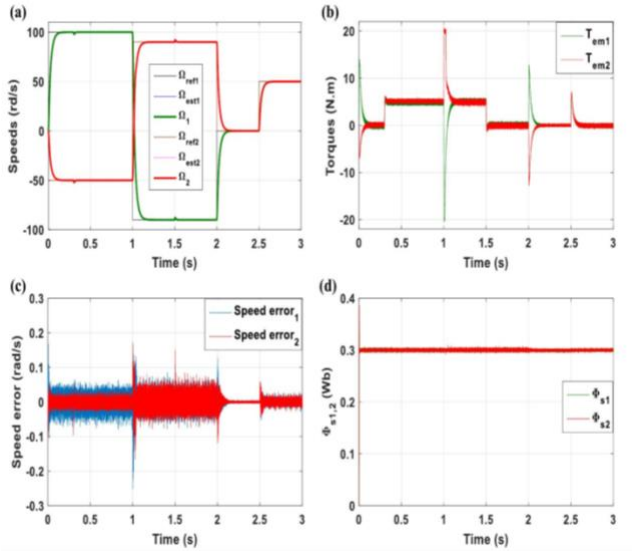


Fig. 9 – Counter-rotating operation: (a) reference/estimated/actual speeds, (b) electromagnetic torques, (c) speed-estimation errors, (d) stator flux magnitudes.

5.3 ALTERNATING HIGH-SPEED REVERSAL

Here the two machines alternate roles every 0.5 s: one accelerates to 100 rad/s under a 5 N·m load while the other is held at standstill with its torque command reduced to zero, and the roles swap at each 0.5 s boundary (Fig. 10). The speed error stays within ≈ 0.05 rad/s at every transition, and — as in the previous two tests — activating or stopping one machine has no visible effect on the other's speed or torque trace, again confirming decoupled control from the shared inverter. Flux remains stable at 0.3 Wb.

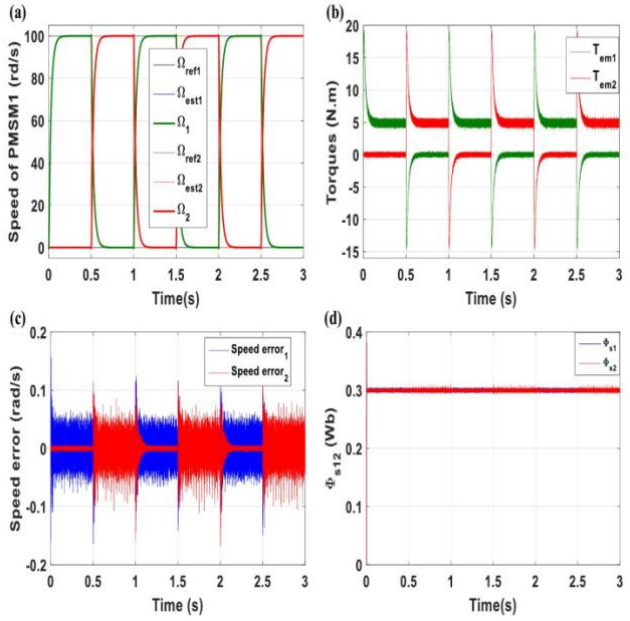


Fig. 10 – Alternating high-speed reversal: (a) reference/estimated/actual speeds, (b) electromagnetic torques, (c) speed-estimation errors, (d) stator flux magnitudes.

5.4 LOW-SPEED OPERATION

Sensorless schemes are typically weakest at low and near-zero speed, so this test drives both machines through small, sign-changing speed references (machine 1: 10, 15, −5, 0, 5, 15 rad/s; machine 2: 5, 15, −5, 10, 5, −5 rad/s, stepped every 0.5 s) with 5 N·m load pulses applied at different instants on each machine. Fig. 11 shows the estimator still tracks both speeds through every sign reversal, including through zero speed, with the speed error kept below 0.02 rad/s — the tightest of all four tests — and the flux again undisturbed at 0.3 Wb.

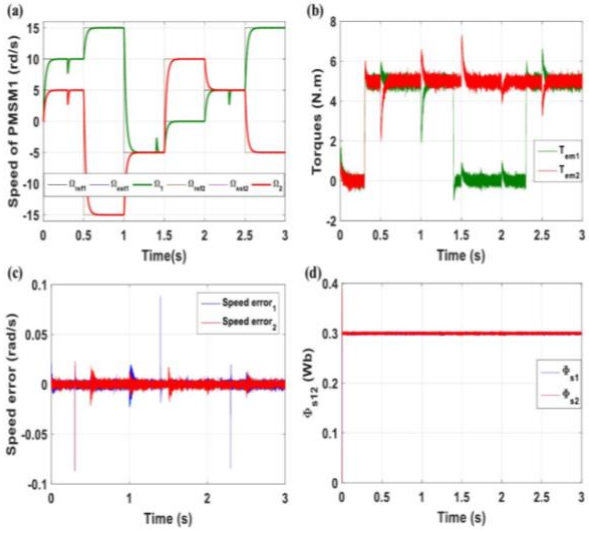


Fig. 11 – Low-speed operation: (a) reference/estimated/actual speeds, (b) electromagnetic torques, (c) speed-estimation errors, (d) stator flux magnitudes.

5.5 CROSS-CUTTING OBSERVATIONS

Three patterns hold consistently across Figs. 8–11. First, the MRAS estimates track the actual speeds closely in every test, including through zero-crossings and direction reversals, confirming that a single per-machine MRAS — built only from the machine's own model — is sufficient even though both machines share one inverter. Second, the generated torque is directly proportional to the q-y-axis inverter currents and is fully decoupled from the d-x-axis currents, so a torque or speed transient on one machine leaves the d-x current, and hence the other machine, unaffected. Third, starting, stopping, reversing, loading, or unloading one machine produces no measurable disturbance on the other's speed, torque, or flux in any of the four tests — direct evidence that the phase-transposition wiring of Section 2.1 achieves complete control decoupling between the two parallel-connected machines from a single five-phase inverter.

5.6 PARAMETER SENSITIVITY AND DC-BUS VOLTAGE LIMITS

The results use the fixed parameters of Table 1 in both the control law and the MRAS model (4); no PIL parameter-sensitivity test was run. From (5), a mismatch between the real stator resistance r_{sj} (temperature-dependent) and its fixed model value enters the r_{sj}/L_{dj} and r_{sj}/L_{qj} terms, slowing speed-error convergence — most strongly at low and near-zero speed (Sec. 5.4), where the back-EMF terms are small. Stability is preserved by the Lyapunov proof of Sec. 3.1, provided the adaptation gains keep their sign; inductance mismatches (L_{dj}, L_{qj}) act similarly. A PIL test with r_{sj}, L_{dj}, Lqj varied by ±10% and ±20% is planned.

Second, both machines share one five-phase inverter, so the applied voltage — the sum of the machine-1 (d–q) and machine-2 (x–y) voltage commands — must stay within the DC-bus voltage envelope. All tests in Sec. 5 satisfy this; however, simultaneous high torque/flux demand at high speed and load may exceed the limit, saturating the modulator, breaking the DTC-SVM command, and losing the d–q / x–y decoupling of Sec. 2.1. Flux-weakening, DC-bus margin, or machine priority rules during saturation are left for future work.

CREDIT AUTHORSHIP CONTRIBUTION STATEMENT

MaamarSOUAIHIA:Methodology, simulation,writing, result analysis, review, editing, original draft.
Kamel TOUNSI: Methodology, result analysis, review, editing.

Received on 10 August 2026

REFERENCES

1. E. Levi, “Multiphase electric machines for variable-speed applications,” IEEE Trans. Ind. Electron., **55**, *5*, pp. 1893–1909 (2008).
2. L. Parsa, H.A. Toliyat, “Five-phase permanent-magnet motor drives,” IEEE Trans. Ind. Appl., **41**, *1*, pp. 30–37 (2005).
3. M. Jones, S.N. Vukosavic, E. Levi, “Parallel-connected multiphase multidrive systems with single inverter supply,” IEEE Trans. Ind. Electron., **56**, *6*, pp. 2047–2057 (2009).
4. Q. Geng, Z. Zhou, G. Zhang, C. Xia, “Sensorless control method for dual permanent magnet synchronous motors driven by five-leg voltage source inverter,” IEEE J. Emerg. Sel. Top. Power Electron., **9**, *5*, pp. 5828–5837 (2021).
5. K.M.S. Benzaoui, E. Benyoussef, A.Z. Kouache, “Three-level direct torque control based on common mode voltage reduction strategy fed two parallel-connected five-phase induction machine,” Rev. Roum. Sci. Techn. – Électrotechn. et Énerg., **69**, *2*, pp. 177–182 (2024).
6. T. Kamel, D. Abdelkader, B. Said, S. Padmanaban, A. Iqbal, “Extended Kalman filter-based sliding mode control of parallel-connected two five-phase PMSM drive system,” Electronics, **7**, *2*, art. 14 (2018).

7. T.G. Habetler, F. Profumo, M. Pastorelli, L.M. Tolbert, "Direct torque control of induction machines using space vector modulation," IEEE Trans. Ind. Appl., **28**, *5*, pp. 1045–1053 (1992).
8. F. Mehedi, I. Bouyakoub, A. Belhamel, "Multi-phase permanent magnet synchronous motor using direct torque adaptive fuzzy control," Rev. Roum. Sci. Techn. – Électrotechn. et Énerg., **70**, *4*, pp. 470–476 (2025).
9. B. Mokhtari, M.A. Moussa, "Neural switching tables for a four-level multicellular inverter to enhance direct torque control of a PMSM," Rev. Roum. Sci. Techn. – Électrotechn. et Énerg., **71**, *1*, pp. 27–32 (2026).
10. I. Assoun, L. Idkhajine, B. Nahid-Mobarakeh, "Wide-speed range sensorless control of five-phase PMSM drive under healthy and open phase fault conditions for aerospace applications," Energies, **16**, *1*, art. 279 (2023).
11. Z. Ider, Y. Bourek, D. Taibi, "Sensorless optimal control of a five-phase induction motor with harmonic minimization," Rev. Roum. Sci. Techn. – Électrotechn. et Énerg., **71**, *1*, pp. 9–14 (2026).
12. H. Kubota, K. Matsuse, "Speed sensorless field-oriented control of induction motor with rotor resistance adaptation," IEEE Trans. Ind. Appl., **30**, *5*, pp. 1219–1224 (1994).
13. C. Hadji, D.E. Khodja, "A sensorless adaptive backstepping sliding mode control of double star induction motor," Rev. Roum. Sci. Techn. – Électrotechn. et Énerg., **71**, *3*, pp. 343–348 (2026).
14. C. Schauder, "Adaptive speed identification for vector control of induction motors without rotational transducers," IEEE Trans. Ind. Appl., **28**, *5*, pp. 1054–1061 (1992).
15. Z. Jiang, R. Leonard, R. Dougal, H. Figueroa, A. Monti, "Processor-in-the-loop simulation, real-time hardware-in-the-loop testing and hardware validation of a digitally-controlled, fuel-cell powered battery-charging station," 2004 IEEE 35th Annual Power Electronics Specialists Conference (PESC), Aachen, Germany, 20–25 June, pp. 2251–2257 (2004).
16. L. Belhamel, A. Buscarino, A. Cucuccio, L. Fortuna, G. Rasconà, "Model-based design streamlines for STM32 motor control embedded software system," 2020 7th International Conference on Control, Decision and Information Technologies (CoDIT), Prague, Czech Republic, June (2020).
17. M. Hu, H. Ahn, J. Park, K. You, "Novel rapid control prototyping for permanent magnet synchronous motor via model-based design and STM32 chip," Int. J. Adv. Manuf. Technol., **135**, art. 104274 (2024).
18. M. Errouha, Q. Combe, S. Motahhir, S.S. Askar, M. Abouhawwash, "Design and processor-in-the-loop implementation of an improved control for IM-driven solar PV-fed water pumping system," Sci. Rep., **12**, art. 4688 (2022).